Finite Element Analysis of MMIC Waveguide Structures with Anisotropic Substrates

Anastasis C. Polycarpou, *Student Member, IEEE*, Michael R. Lyons, *Student Member, IEEE*, and Constantine A. Balanis, *Fellow, IEEE*

Abstract— **This paper presents an extended finite element formulation for a full-wave analysis of biaxial and transverse plane electric and magnetic anisotropic materials with application to monolithic microwave integrated circuits (MMIC's). A convenient formulation of the characteristic impedance based on a power-voltage definition is developed using vector-based finite elements. The resultant generalized eigenvalue problem is solved using a numerically efficient algorithm based on a forward iteration, taking full advantage of the sparsity of the involved matrices. Numerical results are compared and agree well with existing published data for various MMIC configurations. Two specific coplanar waveguide structures, one with a conventional and the other with a suspended substrate, are examined using four common anisotropic materials. Principal axis rotations of the anisotropic substrates are also considered to improve dominant mode dispersion characteristics and minimize higher order mode interactions.**

I. Introduction

ACCURATE prediction of the propagation characteristics in planar structures using anisotropic substrate materials is essential in the design of monolithic microwave integrated circuits (MMIC's) [1]–[5]. Since many substrate materials of interest in microwave and millimeter wave applications exhibit dielectric and/or magnetic anisotropies (such as sapphires, ceramics, and ferrites), the effects due to variations in the material parameters must be fully accounted for. Principal axis rotations of an anisotropic substrate in MMIC's can also lead to significant variations in the effective dielectric constant and characteristic impedance, especially at microwave and millimeter wave frequencies. The dispersive characteristics of coplanar waveguides (CPW's) and other planar structures on single and multilayer isotropic substrates have been extensively analyzed in the literature [6]–[10]. To an extent, the effects due to anisotropy have also been examined; however primarily only for uniaxial and/or biaxial substrates [1], [3], and [5]. Axis rotations in various planes, which introduces off-diagonal elements in the permittivity and/or permeability tensors, were also investigated [2] and [4].

Although quasistatic methods have been employed to analyze the dominant mode characteristics of CPW's and other planar structures on isotropic and anisotropic substrates, such techniques yield accurate results only at very low frequencies [11]. More accurate frequency dependent solutions have been obtained using full-wave analyzes such as the spectral domain approach [2], [3], [10], and the finite element method [12]. While the spectral domain approach is a popular choice for analyzing regular planar structures, the finite element method is more versatile, since it is possible to model arbitrary geometric and material complexities. When using the finite element method, the domain of interest is discretized using simple geometric shapes, such as triangles, where the fields are approximated using linear or higher order basis functions. Because of this, it is also relatively straightforward to compute quantities of interest in MMIC transmission lines, such as total power, voltage difference, and characteristic impedance. A major drawback of the finite element method is the appearance of nonphysical or spurious modes. However, these nonphysical solutions to Maxwell's equations, which appear when using nodal-based finite elements, can be avoided using vector-based finite elements [12]. In addition to imposing tangential continuity of the electric and magnetic fields across element boundaries, the vector finite elements, when implementing the appropriate basis functions, also satisfy the divergence-free condition. Using this type of element, the resulting numerical solutions correspond to the correct physical modes of the structure. Allocation of computer resources is also a major concern when using the finite element method since such a technique requires storage and manipulation of large sparse systems. In this case, sparse linear solvers are usually more suitable than direct solvers [13].

Until now, most finite element method formulations have been used to analyze the propagation characteristics of isotropic and biaxially anisotropic waveguides [12]–[14] with explicit application to only isotropic microstrip structures [12]. In this paper, an extended vector-based finite element formulation for *biaxial and transverse plane anisotropic materials* is presented and used to characterize shielded CPW's with four common anisotropic substrates: sapphire, boron nitride, epsilam-10, and PTFE cloth. A numerically efficient algorithm for finding the largest eigenvalue and eigenvector is presented based on a forward iteration approach. Higher eigenpairs can be found using a Gram–Schmidt orthogonalization process [15]. In addition, an explicit formulation for calculating characteristic impedance applicable to slot-like MMIC structures is given for linear triangular finite elements. Numerical results are compared with existing

Manuscript received August 22, 1995; revised June 14, 1996. This work was supported by the U.S. Army Research Office under Grant DAAL03-92-G-0262.

The authors are with the Department of Electrical Engineering, Telecommunications Research Center, Arizona State University, Tempe, AZ 85287-7206 USA.

Publisher Item Identifier S 0018-9480(96)06901-3.

published data to verify the finite element code. Two specific structures, conventional (C-CPW) and suspended (S-CPW) CPW's, are also analyzed. The dominant and first four higher order modes are examined as a function of substrate material anisotropy and principal axis rotation. Contour plots for the longitudinal fields of the dominant and first higher order modes are also presented for both CPW structures. Visualization of field concentration provides additional physical insight and understanding of the behavior of each propagating mode.

II. Theory

A. Eigen Problem Formulation

A full-wave analysis of shielded waveguide structures, which incorporates both electric and magnetic anisotropic materials, is described by

$$\nabla \times (\bar{\bar{\mu}}_r^{-1} \cdot \nabla \times \mathbf{E}) - k_o^2 \bar{\bar{\epsilon}}_r \mathbf{E} = 0. \tag{1}$$

The permittivity and permeability tensors are assumed to be of the following form:

$$\bar{\bar{\epsilon}}_r = \begin{bmatrix} \epsilon_{xx} & \epsilon_{xy} & 0 \\ \epsilon_{yx} & \epsilon_{yy} & 0 \\ 0 & 0 & \epsilon_{zz} \end{bmatrix}$$

$$\bar{\bar{\mu}}_r = \begin{bmatrix} \mu_{xx} & \mu_{xy} & 0 \\ \mu_{yx} & \mu_{yy} & 0 \\ 0 & 0 & \mu_{zz} \end{bmatrix}$$

$$\bar{\bar{\mu}}_r^{-1} = \begin{bmatrix} \mu_{xx}^{inv} & \mu_{xy}^{inv} & 0 \\ \mu_{yx}^{inv} & \mu_{yy}^{inv} & 0 \\ 0 & 0 & \mu_{zz}^{inv} \end{bmatrix}.$$

The inverse of the permeability tensor is calculated using symbolic manipulations of a 3×3 square matrix. It is also assumed that there are no current sources in the domain of interest and that the corresponding boundary conditions are given by

$$\hat{n} \times \mathbf{E} = 0 \quad \text{on an electric wall} \tag{2}$$

$$\hat{n} \times (\nabla \times \mathbf{E}) = 0 \quad \text{on a magnetic wall.} \tag{3}$$

The representative variational functional for such a problem can be expressed as

$$F(\mathbf{E}) = \tfrac{1}{2} \iint_\Omega [(\nabla \times \mathbf{E}) \bar{\bar{\mu}}_r^{-1} (\nabla \times \mathbf{E})^* - k_o^2 \mathbf{E} \bar{\bar{\epsilon}}_r \mathbf{E}^*] \, d\Omega. \tag{4}$$

Assuming that the dependence of the fields in the z-direction is $e^{-jk_z z}$, the functional can be written in terms of the transverse and the longitudinal fields similar to [12]; i.e.,

$$\begin{aligned} F(\mathbf{E}) = \tfrac{1}{2} \iint_\Omega & [(\nabla_t \times \mathbf{E}_t) \tilde{\tilde{\mu}}_r (\nabla_t \times \mathbf{E}_t)^* \\ & - k_o^2 (\mathbf{E}_t \bar{\bar{\epsilon}}_r \mathbf{E}_t^* + E_z \bar{\bar{\epsilon}}_r E_z^*) \\ & + (\nabla_t E_z + jk_z \mathbf{E}_t) \tilde{\tilde{\mu}}_r (\nabla_t E_z + jk_z \mathbf{E}_t)^*] \, d\Omega \end{aligned} \tag{5}$$

where ∇_t is the transverse del operator, $\mathbf{E}_t$ is the transverse component of the electric field, and E_z is the longitudinal component of the electric field. The tensor $\tilde{\tilde{\mu}}_r$, referred to as the relative pseudo-permeability, has also been introduced and is defined as

$$\tilde{\tilde{\mu}}_r = \begin{bmatrix} \mu_{yy}^{inv} & -\mu_{yx}^{inv} & 0 \\ -\mu_{xy}^{inv} & \mu_{xx}^{inv} & 0 \\ 0 & 0 & \mu_{zz}^{inv} \end{bmatrix}. \tag{6}$$

If an isotropic permeability is assumed, the functional is reduced to the one given in [12]. Referring to Fig. 1, these field components can be subsequently expanded as a summation of scalar and vector basis functions

$$\begin{aligned} \mathbf{e}_t &= k_z \mathbf{E}_t \\ &= \sum_{i=1}^{n} \mathbf{N}_i^e e_{ti}^e \end{aligned} \tag{7}$$

$$\begin{aligned} e_z^e &= -jE_z \\ &= \sum_{i=1}^{n} N_i^e e_{zi}^e \end{aligned} \tag{8}$$

where n represents the number of degrees of freedom in each element. The functional given in (5) can be discretized, using a procedure similar to [12] to obtain the following elemental matrices:

$$\begin{aligned} [A_{tt}^e]_{ij} &= \iint_\Omega [\{\nabla_t \times \mathbf{N}_i^e\}^T \tilde{\tilde{\mu}}_r \{\nabla_t \times \mathbf{N}_j^e\} \\ &\quad - k_o^2 \{\mathbf{N}_i^e\}^T \bar{\bar{\epsilon}}_r \{\mathbf{N}_j^e\}] \, d\Omega \\ &= [S_{tt}^e]_{ij} - k_o^2 [T_{tt}^e]_{ij} \end{aligned} \tag{9}$$

$$\begin{aligned} [B_{tt}^e]_{ij} &= \iint_\Omega \{\mathbf{N}_i^e\}^T \tilde{\tilde{\mu}}_r \{\mathbf{N}_j^e\} \, d\Omega \\ &= [T_{tt}^e]_{ij}, \quad \text{where} \quad \bar{\bar{\epsilon}}_r \Rightarrow \tilde{\tilde{\mu}}_r \end{aligned} \tag{10}$$

$$[B_{tz}^e]_{ij} = \iint_\Omega \{\mathbf{N}_i^e\}^T \tilde{\tilde{\mu}}_r \{\nabla_t N_j^e\} \, d\Omega \tag{11}$$

$$[B_{zt}^e]_{ij} = \iint_\Omega \{\nabla_t N_i^e\}^T \tilde{\tilde{\mu}}_r \{\mathbf{N}_j^e\} \, d\Omega \tag{12}$$

$$\begin{aligned} [B_{zz}^e]_{ij} &= \iint_\Omega [\{\nabla_t N_i^e\}^T \tilde{\tilde{\mu}}_r \{\nabla_t N_j^e\} \\ &\quad - k_o^2 \{N_i^e\}^T \bar{\bar{\epsilon}}_r \{N_j^e\}] \, d\Omega \\ &= [S_{zz}^e]_{ij} - k_o^2 [T_{zz}^e]_{ij} \end{aligned} \tag{13}$$

where i and j denote the row and column, respectively, of the corresponding entry; the size of the elemental matrices is $n \times n$. Closed form expressions for the above matrices are given explicitly, for the case of linear triangular elements, in the Appendix. Although the derivation of these equations is rather tedious and involved, their computer implementation is straightforward. Following the assembly of all elements in the finite element region, a generalized eigenvalue system is formed

$$\begin{bmatrix} A_{tt} & 0 \\ 0 & 0 \end{bmatrix} \begin{Bmatrix} e_t \\ e_z \end{Bmatrix} = -k_z^2 \begin{bmatrix} B_{tt} & B_{tz} \\ B_{zt} & B_{zz} \end{bmatrix} \begin{Bmatrix} e_t \\ e_z \end{Bmatrix}. \tag{14}$$

This can be solved using either a standard direct solver or an iterative solver. The former usually results in the computation of all the eigenvalues and eigenvectors of the matrix system. However, in practice, only the first few dominant modes

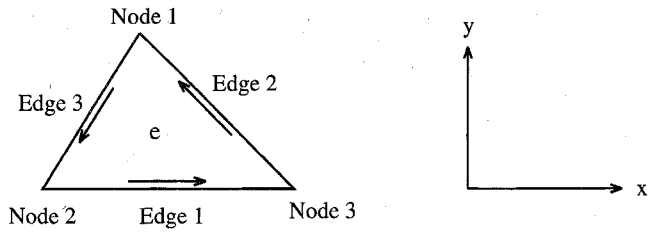

Fig. 1. Triangular vector element.

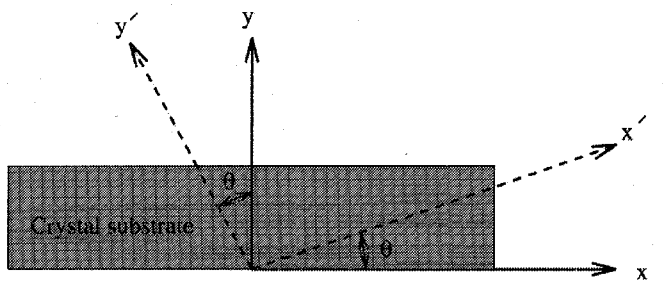

Fig. 2. Definition of principal axis rotation for an anisotropic substrate.

are desired; therefore, an iterative solver is usually more appropriate.

To account for principal axis rotation of anisotropic substrates, the permittivity tensor, $\bar{\bar{\epsilon}}_r$, needs to be modified according to Fig. 2. Assuming that

$$\bar{\bar{\epsilon}}_r' = \begin{bmatrix} \epsilon_1 & 0 & 0 \\ 0 & \epsilon_2 & 0 \\ 0 & 0 & \epsilon_3 \end{bmatrix}$$

for a biaxial substrate, the resulting permittivity tensor, $\bar{\bar{\epsilon}}_r$, for any angle of rotation θ is given by

$$\bar{\bar{\epsilon}}_r = \begin{bmatrix} \epsilon_{xx} & \epsilon_{xy} & 0 \\ \epsilon_{yx} & \epsilon_{yy} & 0 \\ 0 & 0 & \epsilon_{zz} \end{bmatrix}$$

where

$$\epsilon_{xx} = \epsilon_1 \cos^2(\theta) + \epsilon_2 \sin^2(\theta) \tag{15}$$

$$\epsilon_{yy} = \epsilon_1 \sin^2(\theta) + \epsilon_2 \cos^2(\theta) \tag{16}$$

$$\epsilon_{zz} = \epsilon_3 \tag{17}$$

$$\epsilon_{xy} = \epsilon_{yx} = (\epsilon_2 - \epsilon_1) \sin(\theta) \cos(\theta). \tag{18}$$

In this paper, the crystal lattice is rotated only from 0–90°.

B. Characteristic Impedance Formulation

After solving the eigenvalue problem given in (14) at each frequency point, the propagation constant in the z-direction and the corresponding normalized transverse and longitudinal fields inside the structure can be obtained. Both the propagation constant and the fields are needed for the calculation of the characteristic impedance. Although the definition of the characteristic impedance is not unique for inhomogeneous waveguide structures, the voltage-power definition was chosen for the present analysis. The corresponding expression is given by [5]

$$Z_c = \frac{VV^*}{2P}, \quad P = \sum_{i=1}^{N} P_i \tag{19}$$

where V is the voltage difference in the slot, P_i is the power calculated in each element, P is the total power flowing in the z-direction, and N is the number of finite elements in the domain of interest. The elemental power P_i is given by the Poynting vector

$$P_i = \tfrac{1}{2}\,\mathrm{Re}\left[\iint_{\triangle} \mathbf{E}_i \times \mathbf{H}_i^* \cdot \hat{a}_z \, ds\right] = \tfrac{1}{2}\mathrm{Re}\left[\iint_{\triangle} (E_x H_y^* - E_y H_x^*)\, ds\right] \tag{20}$$

where the magnetic field components H_x and H_y are calculated directly from Maxwell's equations; note that the expressions for the electric field components are known in closed form. The above integration is performed over the area of each finite element.

Based on a linear triangular element formulation, where the edges represent transverse fields and the nodes represent longitudinal fields, the final expressions for the transverse components of both the electric and magnetic fields are explicitly given by

$$E_x(x, y) = C_1 - C_2 y \tag{21}$$

$$E_y(x, y) = C_3 x - C_4 \tag{22}$$

$$H_x(x, y) = D_1 y + D_2 x + D_3 \tag{23}$$

$$H_y(x, y) = D_4 y + D_5 x + D_6 \tag{24}$$

where C_{1-4} and D_{1-6} are constants defined as

$$C_1 = \frac{1}{2A}\sum_{i=1}^{3} l_i y_i e_{ti}^e$$

$$C_2 = \frac{1}{2A}\sum_{i=1}^{3} l_i e_{ti}^e \tag{25}$$

$$C_3 = \frac{1}{2A}\sum_{i=1}^{3} l_i e_{ti}^e$$

$$C_4 = \frac{1}{2A}\sum_{i=1}^{3} l_i x_i e_{ti}^e \tag{26}$$

$$D_1 = \frac{-\mu_{xy}^{inv} k_z}{2A\omega\mu_o}\sum_{i=1}^{3} l_i e_{ti}^e$$

$$D_2 = \frac{-\mu_{xx}^{inv} k_z}{2A\omega\mu_o}\sum_{i=1}^{3} l_i e_{ti}^e \tag{27}$$

$$D_4 = \frac{-\mu_{yy}^{inv} k_z}{2A\omega\mu_o}\sum_{i=1}^{3} l_i e_{ti}^e$$

$$D_5 = \frac{-\mu_{yx}^{inv} k_z}{2A\omega\mu_o}\sum_{i=1}^{3} l_i e_{ti}^e \tag{28}$$

$$D_3 = \frac{j}{2A\omega\mu_o}\left[-\mu_{xy}^{inv}\left(\sum_{i=1}^{3} b_i e_{zi}^e\right) - j\mu_{xy}^{inv}k_z\left(\sum_{i=1}^{3} l_i y_i e_{ti}^e\right) + \mu_{xx}^{inv}\left(\sum_{i=1}^{3} c_i e_{zi}^e\right) - j\mu_{xx}^{inv}k_z\left(\sum_{i=1}^{3} l_i x_i e_{ti}^e\right)\right] \quad (29)$$

$$D_6 = \frac{j}{2A\omega\mu_o}\left[+\mu_{yx}^{inv}\left(\sum_{i=1}^{3} c_i e_{zi}^e\right) - j\mu_{yx}^{inv}k_z\left(\sum_{i=1}^{3} l_i x_i e_{ti}^e\right) - \mu_{yy}^{inv}\left(\sum_{i=1}^{3} b_i e_{zi}^e\right) - j\mu_{yy}^{inv}k_z\left(\sum_{i=1}^{3} l_i y_i e_{ti}^e\right)\right] \quad (30)$$

where x_i and y_i $(i = 1, 2, 3)$ denote the coordinates of each triangular element, l_i $(i = 1, 2, 3)$ denote the lengths of the individual edges, and A denotes the area of the triangular element which is given by

$$A = \tfrac{1}{2}\{x_1 b_1 + x_2 b_2 + x_3 b_3\}. \quad (31)$$

Also, the b_i's and c_i's are defined as

$$\begin{aligned} b_1 &= y_2 - y_3 \\ b_2 &= y_3 - y_1 \\ b_3 &= y_1 - y_2 \\ c_1 &= x_3 - x_2 \\ c_2 &= x_1 - x_3 \\ c_3 &= x_2 - x_1. \end{aligned}$$

The integration in (20), over the area of the triangular element, can be evaluated very conveniently using the simplex coordinates.

In addition to calculating the total power flowing through the waveguide structure at each frequency point, the voltage difference in the slot, defined by

$$V = -\int_L \mathbf{E}\cdot d\mathbf{l} \quad (32)$$

needs to be determined. Assuming that the slot lies horizontally, the above integral can be simplified to

$$V = -\int_{x_l}^{x_r} E_x\, dx \quad (33)$$

where x_l and x_r are the left and right x-coordinates of the slot. Since the slot is discretized into finite linear triangular elements, the line integral has to be evaluated for each element in the slot. The total voltage difference is given by

$$V = \sum_{i=1}^{N_s} V_i \quad (34)$$

where N_s is the number of elements in the slot and V_i is the individual voltage difference. Using linear triangular elements, this can be expressed as

$$V_i = \frac{1}{2A}(x_r^e - x_l^e)[(y_1 - h)l_1 e_{t1} + (y_2 - h)l_2 e_{t2} + (y_3 - h)l_3 e_{t3}] \quad (35)$$

where x_r^e and x_l^e are the limits of the voltage line integral evaluated for each element in the slot, and h is the height of the slot.

C. A Generalized Eigenvalue Solver

The solution of a generalized eigenvalue problem defined as

$$[K]\{x\} = \lambda[M]\{x\} \quad (36)$$

can be computationally intensive and time demanding, especially as the number of unknowns increases. There are various methods of solving for both the eigenvalues and the corresponding eigenvectors. The simplest method is to store both matrices in a full format and then use a direct solver, like those available in EISPACK [16]. Such a solver usually computes all the eigenvalues and eigenvectors of the matrix system. This approach, however, is very inefficient both in terms of computational time and memory requirements. One of the most suitable methods for solving a generalized eigenvalue problem is the power iteration, otherwise known as forward and inverse power iteration. Note that the forward power iteration is used to estimate the largest eigenvalues of the matrix system, whereas the inverse power iteration is used to estimate the lowest eigenvalues. The major advantages of using a power iteration are: first, speed-up in computational time; second, complete utilization of the sparsity of the matrices; third, computation of only a selected number of eigenvalue/eigenvector pairs. As far as the latter is concerned, it is important to realize that in analyzing waveguide structures, only the most dominant modes are significant; therefore, it is not necessary that all higher order eigenvalues and eigenvectors be calculated. In addition, the accuracy of the higher order eigenvalues and eigenvectors deteriorates accordingly, which is another reason for not calculating more than a few eigenmodes.

The results presented in this paper were obtained using a forward power iteration method. The algorithm is quite simple but very powerful. The major steps involved in the algorithm are the following:

Step 1:

- Initialize a starting vector $\mathbf{u}^{(0)}$ (other than the zero vector).
- Set the iteration index $k = 0$.

Step 2:

- Increment the iteration index; $k = k + 1$.

Step 3:

- Determine a vector $\mathbf{v}^{(k-1)} = K\mathbf{u}^{(k-1)}$.

For efficiency, the multiplication of a matrix with a vector can be carried out using a sparse format.

Step 4:

- Solve the linear system $M\,\mathbf{u}^{(k)} = \mathbf{v}^{(k-1)}$.

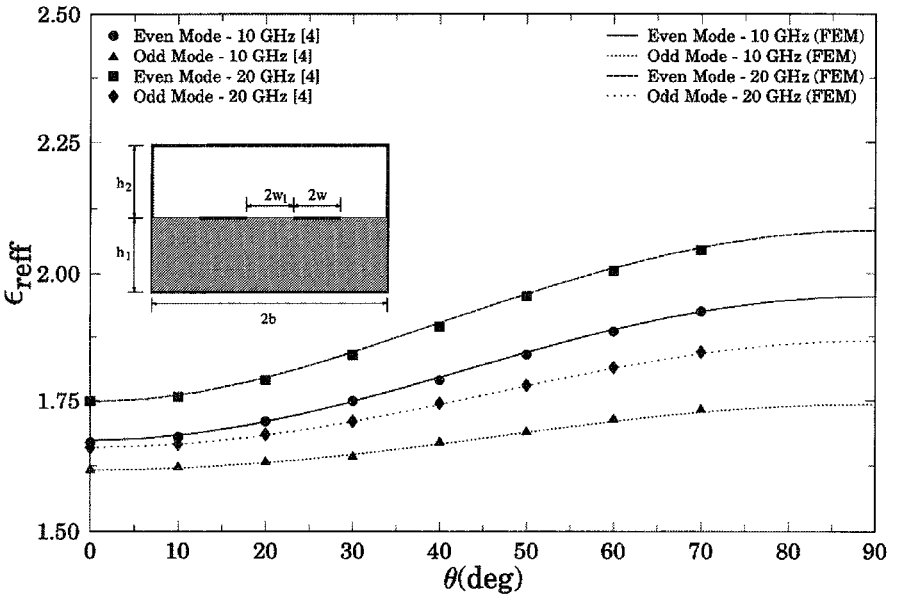

Fig. 3. Dispersion curves for the dominant mode of a coupled microstrip lines on a boron nitride substrate ($\epsilon_{xx} = 5.12$, $\epsilon_{yy} = 3.4$, and $\epsilon_{zz} = 5.12$); $h_1 = 1.5$ mm, $w = w_1 = 0.75$ mm, and $2b = 8.5$ mm.

An efficient way to solve the above linear system is to use a sparse LU solver, such as *SPARSE 1.3a* [17]. The advantage of using such a solver is that the factorization of the M matrix needs to be performed only once; therefore, subsequent iterations require only backward substitution which results in significant speed-up of the algorithm. Other solvers, such as the ones that use iterative techniques, are also appropriate since the sparsity of the matrix can be utilized efficiently.

Step 5:

- Assign $\mathbf{v}^{(k)} = K\mathbf{u}^{(k)}$.

Step 6:

- Estimate the largest eigenvalue using $\lambda^{(k)} = \mathbf{u}^{*(k)}\mathbf{v}^{(k)}/(\mathbf{u}^{*(k)}\mathbf{v}^{(k-1)})$.

The symbol "*" denotes conjugate transpose.

Step 7:

- Normalize the corresponding eigenvector as follows: $\mathbf{u}^{(k)} = \mathbf{u}^{(k)}/\sqrt{\mathbf{u}^{*(k)}\mathbf{v}^{(k-1)}}$.

Step 8:

- Calculate the 2-norm of the residual: $\|R\|_2^{(k)} = \|K\,\mathbf{u}^{(k)} - \lambda M\mathbf{u}^{(k)}\|_2$.
- If $\|R\|_2^{(k)} \leq$ tolerance $\Rightarrow$ Exit the algorithm; otherwise, go to Step 1.

As it was already mentioned, the above algorithm converges to the largest eigenvalue, provided that the starting vector does not coincide with one of the eigenvectors. In order to be able to find higher order eigenvalues, the starting vector has to be chosen from a space M orthogonal to the already calculated eigenvectors. Such an orthogonalization is well-known as the Gram–Schmidt process [15]. In other words, if $\mathbf{U}_1, \mathbf{U}_2, \cdots, \mathbf{U}_m$ are considered the first m eigenvectors already calculated using the power iteration, the starting vector for each iteration, according to the Gram–Schmidt orthogonalization, is given by

$$\mathbf{u}^{k-1} = \mathbf{u}^{k-1} - [\mathbf{u}^{*(k-1)}M\mathbf{U}_1]^*\mathbf{U}_1 - [\mathbf{u}^{*(k-1)}M\mathbf{U}_2]^*\mathbf{U}_2 - \cdots - [\mathbf{u}^{*(k-1)}M\mathbf{U}_m]^*\mathbf{U}_m. \quad (37)$$

Using this as a starting vector in each iteration will result in the calculation of λ_{m+1} and $\mathbf{U}_{m+1}$. Note that the accuracy of the algorithm can be improved by setting the convergence tolerance to a lower value. It is also important to mention here that the forward power iteration converges much faster than the inverse power iteration [12], at least for the type of problems considered in this paper, which is another significant reason for implementing this particular algorithm.

III. Results

A complete FEM code based on the analytical formulation presented in the previous section was written and tested for a variety of geometries and materials. The FEM code was interfaced with SDRC I-DEAS [18], a software package from Structural Dynamics Research Corporation with preprocessing requirements such as meshing, material definition, and boundary conditions. It was also interfaced with other well-known packages such as PLOTMTV and GEOMVIEW which can be used for data visualization and important geometry checks.

The first geometry considered in validating the finite element formulation and corresponding code was the coupled microstrip lines initially examined by Mostafa *et al.* [4] using a spectral domain approach. The coupled microstrip lines rest on a uniaxial boron nitride substrate ($\epsilon_{xx} = \epsilon_{zz} = 5.12$, $\epsilon_{yy} = 3.4$). The effective dielectric constant, ϵ_{reff}, versus a principal axis crystal rotation angle, θ, as defined in [4], is depicted in Fig. 3 for two different frequencies: $f = 10$ GHz and $f = 20$ GHz. A comparison between our results and data

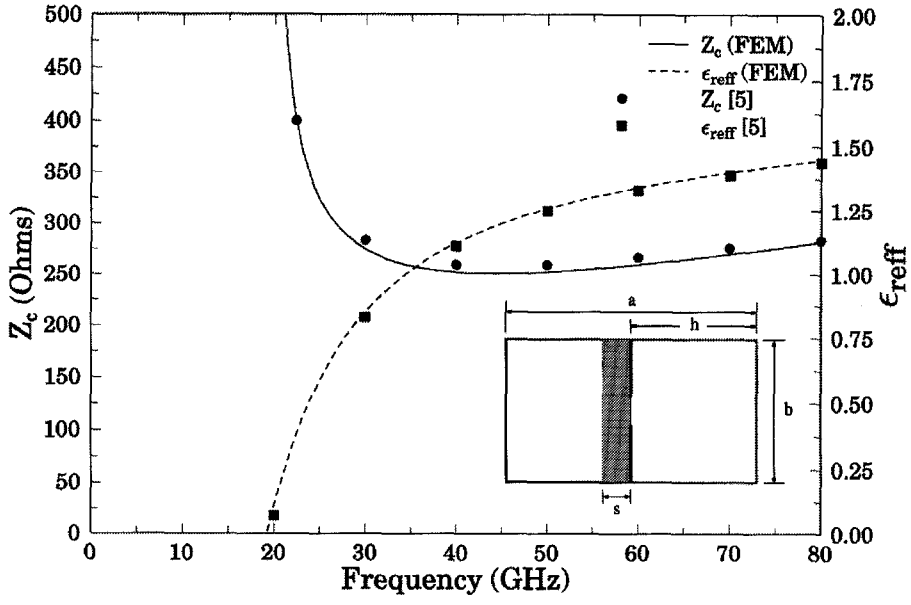

Fig. 4. Characteristic impedance versus frequency for a unilateral finline; $a = 2b = 4.7752$ mm, $s = 0.127$ mm, $h = 2.3876$ mm, $d = 0.47752$ mm, and $\epsilon_r = 3.8$.

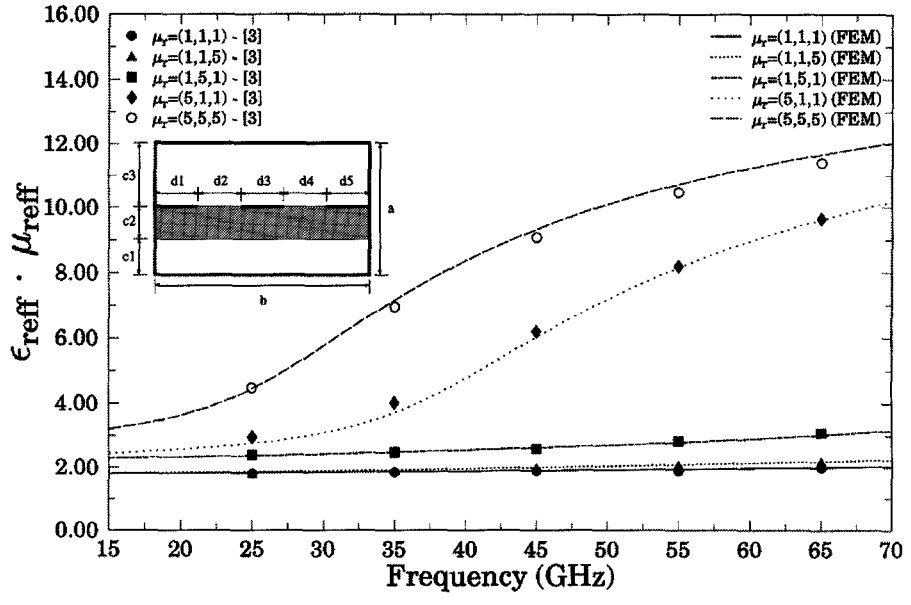

Fig. 5. Dispersion curves for the dominant mode of a suspended coplanar waveguide; $a = 7.112$ mm, $b = 3.556$ mm, $c_1/a = 0.4$, $c_2/a = 0.1$, $c_3/a = 0.5$, and $d_1 = d_2 = d_3 = d_4 = d_5 = b/5$.

obtained from [4] shows a very good agreement between the two methods.

A second geometry considered was a unilateral finline already examined by Mansour *et al.* [5]. The frequency dependence of the effective dielectric constant ϵ_{reff} and the characteristic impedance Z_c is illustrated in Fig. 4. Data obtained from the corresponding figure in [5] are also shown on the same graph. The agreement between the two sets of data is very good. It is important to mention here that the accuracy of the characteristic impedance depends on the mesh density in the finite element region, especially near the slot. The reason is due to the fact that the formulation of the characteristic impedance involves the actual field distribution in the entire structure. Specifically, fields in the vicinity of the slot, which are known to exhibit rapid spatial variations, require either a finer mesh or higher order elements for good representation. In obtaining the results shown in Fig. 4, 13 linear triangular elements were used across the slot and a total of 1036 elements in the entire structure.

A suspended coplanar waveguide with magnetic anisotropic uniaxial substrates was also analyzed using the finite element code. This geometry was initially examined by Mazé-Merceur *et al.*, [3] using the spectral domain approach. Defining the quantity $\epsilon_{reff} \cdot \mu_{reff} = (k_z/k_o)^2$ [3], the effects

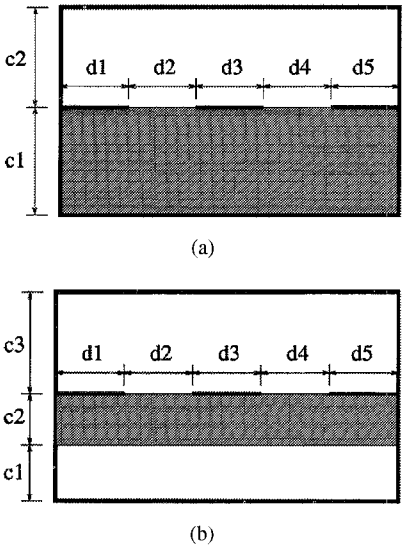

Fig. 6. Conventional and suspended waveguide geometries: (a) $c_1 = 3.2$ mm, $c_2 = 2.71$ mm, $d_1 = d_5 = 1.5$ mm, $d_2 = d_3 = d_4 = 0.5$ mm and (b) $c_1 = 2.7$ mm, $c_2 = 0.5$ mm, $c_3 = 2.71$ mm, $d_1 = d_5 = 1.5$ mm, and $d_2 = d_3 = d_4 = 0.5$ mm.

due to both electric and magnetic anisotropy are accounted for. A comparison of the $\epsilon_{reff} \cdot \mu_{reff}$ versus frequency between the two methods is illustrated in Fig. 5 for a variety of isotropic and uniaxially magnetic anisotropic substrates. A good agreement is observed between the two sets of data.

After verifying the finite element formulation and corresponding code, the effective dielectric constant and the characteristic impedance versus frequency of a conventional coplanar waveguide were investigated. The geometry is depicted in Fig. 6(a) using four commonly used uniaxial/biaxial anisotropic substrates: sapphire ($\epsilon_{xx} = \epsilon_{zz} = 9.4$, $\epsilon_{yy} = 11.6$), epsilam-10 ($\epsilon_{xx} = \epsilon_{zz} = 13.0$, $\epsilon_{yy} = 10.3$), boron nitride ($\epsilon_{xx} = \epsilon_{zz} = 5.12$, $\epsilon_{yy} = 3.4$), and PTFE cloth ($\epsilon_{xx} = 2.89$, $\epsilon_{yy} = 2.45$, $\epsilon_{zz} = 2.95$). The relative permeability of all these crystals is assumed unity. The corresponding graphs are illustrated in Fig. 7.

Starting with sapphire in Fig. 7, it is interesting to observe that the dominant mode is very dispersive. The corresponding ϵ_{reff} varies by as much as 100% within the 100 GHz range shown in the figure. The dispersive behavior of the dominant mode occurs within the range of 10–30 GHz, which limits the single mode operational bandwidth. Within the same frequency range, the corresponding characteristic impedance of the dominant mode exhibits a rapid decrease toward zero. In addition, the dominant mode shows very little coupling with the first four HOMs; however, there is a strong coupling between the first and second HOM's. As a result of such a strong interaction between these two modes, the characteristic impedance of the first HOM is only shown up to a frequency of about 15 GHz, where significant coupling is observed. Coupling between any two modes is present when the corresponding phase velocities or propagation constants are nearly the same. The closer these quantities are, the stronger the coupling between the two modes.

Without discussing the remaining three sets of graphs in Fig. 7 in detail, it is interesting to note that besides the HOM coupling effects, there is an additional strong interaction between the dominant mode and the HOM's. By examining the field distribution of the dominant mode in the coplanar waveguide at various frequencies, it was realized that this mode actually *crosses* with a number of HOM's. Although such a process is cumbersome and time consuming, it is the only way of tracking down the individual modes within a given frequency range. This type of dispersion effect, in addition to the dominant mode dispersion characteristics, further limits the single mode operation of the structure. A comparison of the percent change in the effective dielectric constant of the dominant mode within a range of 100 GHz for all four substrates is summarized in Table I. The sapphire substrate appears to exhibit the highest percent change in ϵ_{reff}, whereas the PTFE cloth exhibits the lowest. The characteristic impedance of the dominant mode remains relatively constant for all four cases up to a frequency where the dispersion effect becomes quite significant. At that frequency, the characteristic impedance of the dominant mode begins to decay toward zero. On the other hand, the first HOM corresponds to a slot-line like mode [10] and, therefore, the characteristic impedance asymptotically approaches infinity at frequencies near the cutoff frequency.

The dispersion curves concerning the conventional coplanar waveguide were characterized by a strong interaction between the dominant mode and HOM's, which clearly restrains the single mode operation in MMIC's. Furthermore, the relatively high percent change in the effective dielectric constant within the 100 GHz frequency range introduces additional unwanted dispersion. These problems can be overcome by introducing a single layer suspended coplanar waveguide as shown in Fig. 6(b). The effective dielectric constant of the first five most dominant modes and the characteristic impedance of the first two most dominant modes were computed and are shown in Fig. 8. Without discussing each graph individually, it is clear that there is a significant improvement in the effective dielectric constant and characteristic impedance of the current geometry compared to those corresponding to the conventional coplanar waveguide. First, the dispersive nature of the dominant mode for all four types of substrate is significantly reduced. The corresponding percent change in ϵ_{reff} is tabulated in Table I. The dominant mode when using sapphire, epsilam-10, and boron nitride still exhibits some interaction with HOM's, but clearly this mode interaction occurs at frequencies much higher than those corresponding to the conventional coplanar waveguide. On the contrary, the dominant mode when using PTFE cloth, in addition to having the less dispersive characteristics, shows no interaction with any HOM, at least in a frequency range of 100 GHz. Furthermore, the cutoff frequencies for both the first and second HOM's have shifted to a higher frequency. In particular, the cutoff frequency of the second HOM, in all four cases examined, shifts to a frequency of about 30 GHz, which is important for wideband operation in MMIC designs.

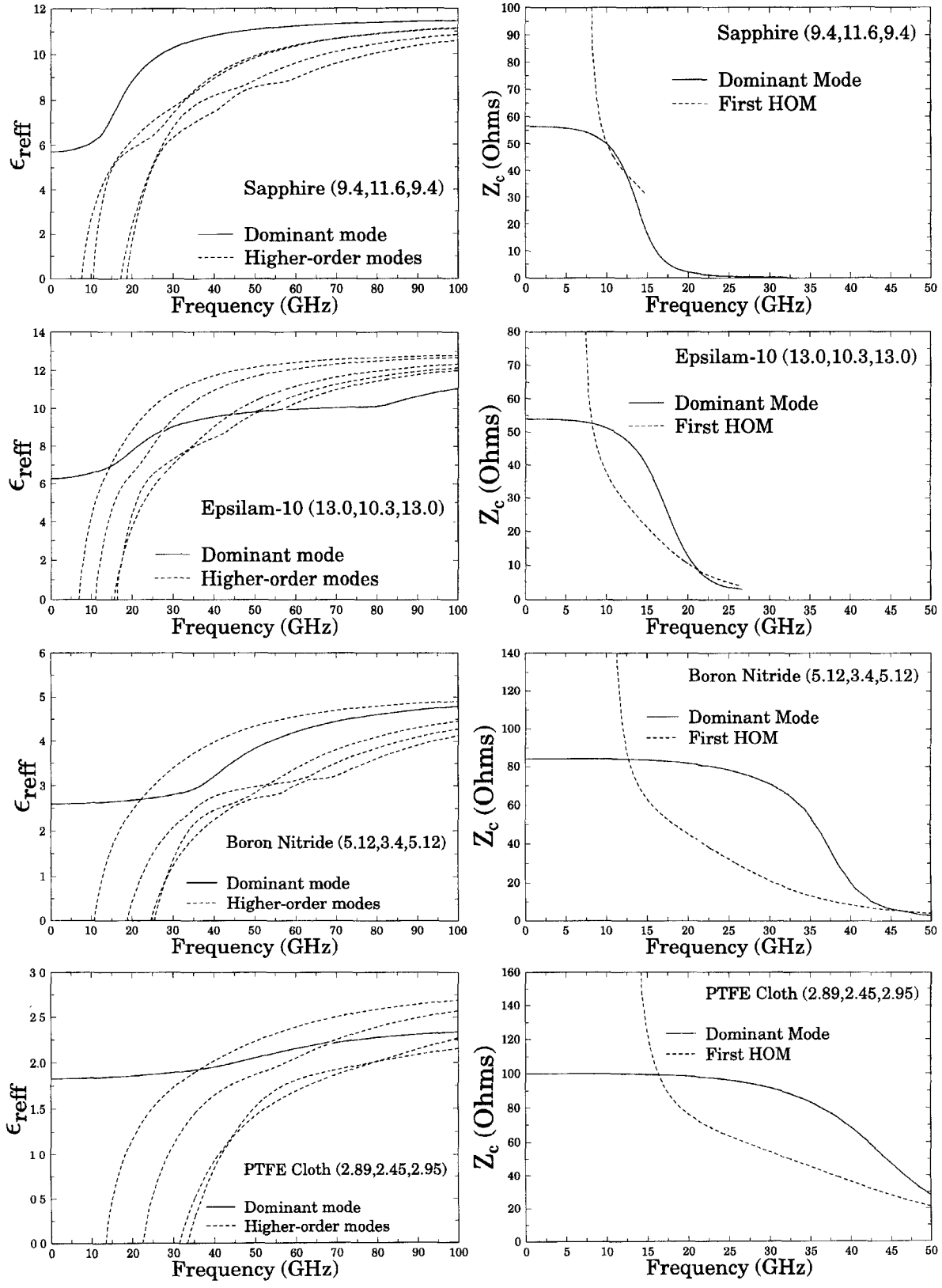

Fig. 7. Effective dielectric constant and characteristic impedance curves of a conventional CPW using anisotropic substrates.

By introducing resistive films in the structure [19], the first HOM can be considerably attenuated, thereby increasing the single mode bandwidth to approximately 30 GHz which is a significant improvement to that of the conventional coplanar waveguide.

TABLE I
PERCENTAGE CHANGE IN THE EFFECTIVE DIELECTRIC CONSTANT WITHIN A RANGE 100 GHz

Structure	Sapphire	Epsilam-10	Boron Nitride	PTFE Cloth
C-CPW	+100%	+75%	+85%	+60%
S-CPW	+83%	+67%	+26%	+9%

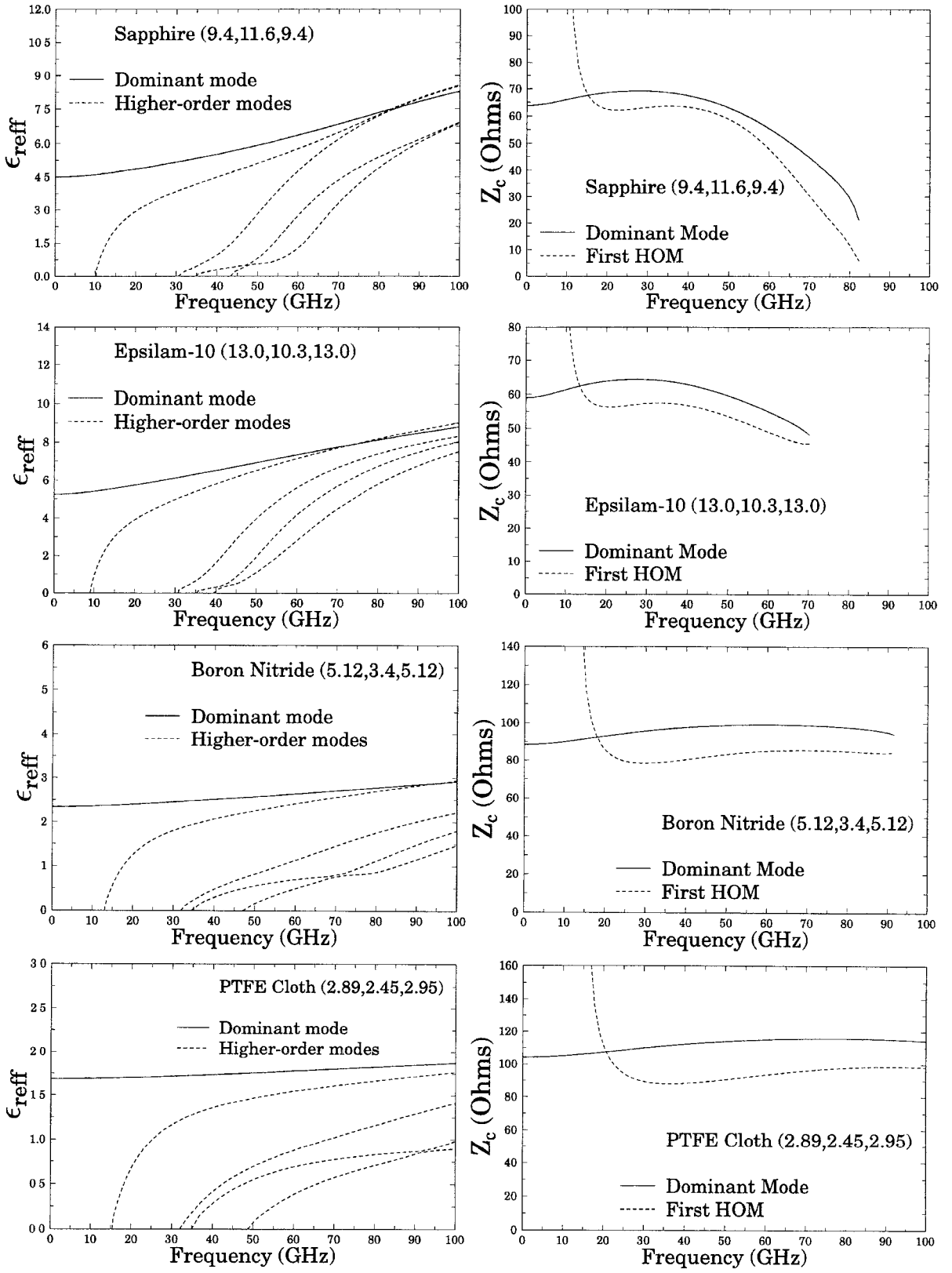

Fig. 8. Effective dielectric constant and characteristic impedance curves of a suspended CPW using anisotropic substrates.

The dispersion characteristics of the suspended coplanar waveguide can be further altered by rotating the crystal lattice in the transverse plane while observing the variation of the ϵ_{reff} and Z_c at a certain frequency. Considering only the dominant and the first HOM at a frequency of 50 GHz, the rotation angle θ is varied from 0 to 90°. Based on our experience, effects on the propagation characteristics, such as ϵ_{reff} and Z_c, are most noticeable only at relatively high

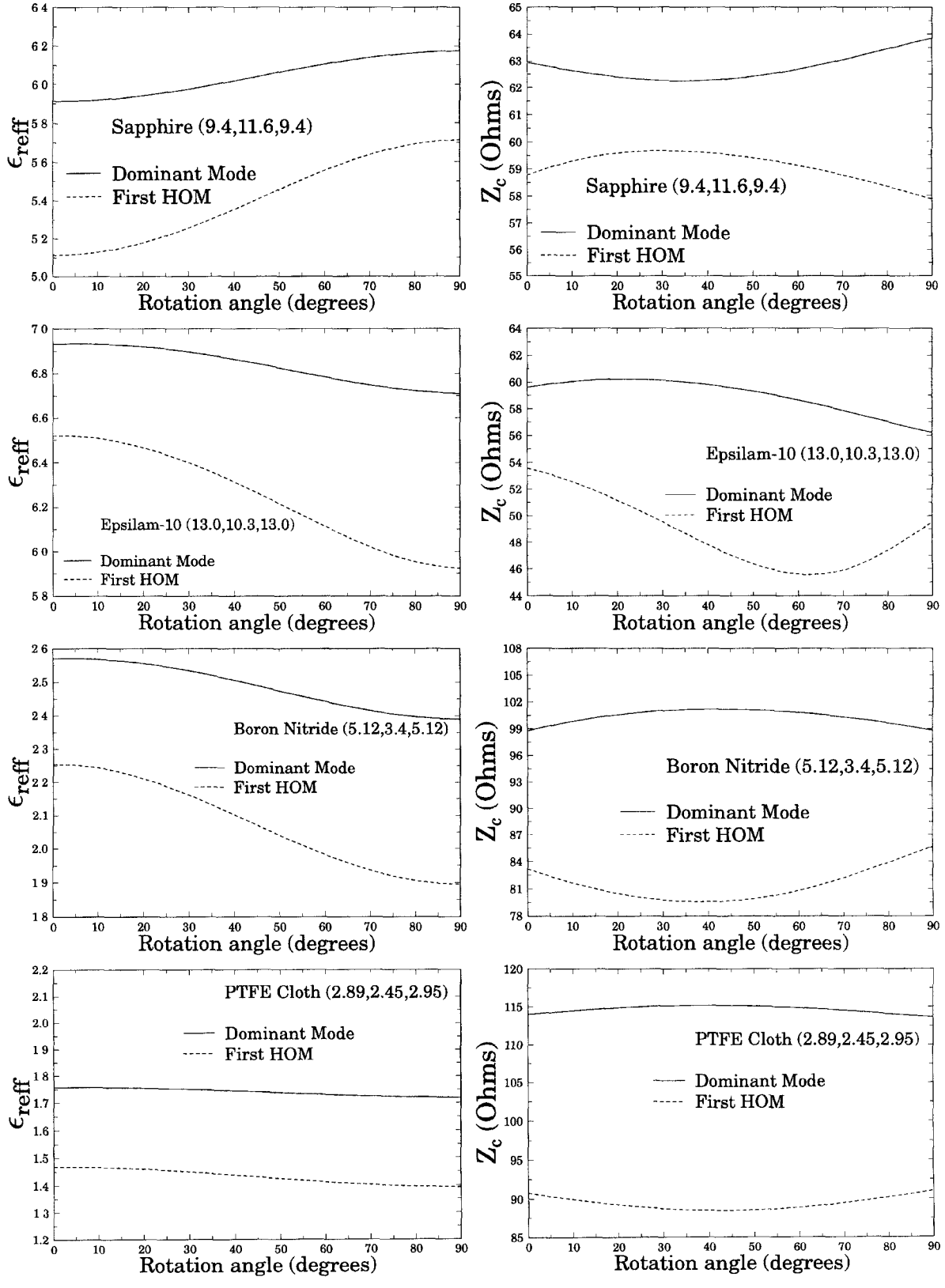

Fig. 9. The effect of crystal rotation on the effective dielectric constant and characteristic impedance of a suspended CPW at a frequency of 50 GHz.

TABLE II
PERCENTAGE CHANGE IN THE EFFECTIVE DIELECTRIC CONSTANT BY ROTATING THE CRYSTAL LATTICE 90° AT A FREQUENCY OF 50 GHz (S-CPW)

Mode	Sapphire	Epsilam-10	Boron Nitride	PTFE cloth
Dominant	+4.4%	−3.2%	−7.0%	−2.3%
First HOM	+11.7%	−9.2%	−16.0%	−5.4%

frequencies. The corresponding results due to crystal rotation for all four substrates are shown in Fig. 9. When using sapphire, the effective dielectric constant of the dominant mode increases with angle of rotation θ which, according to Fig. 7, will result in a more dispersive structure. The increase

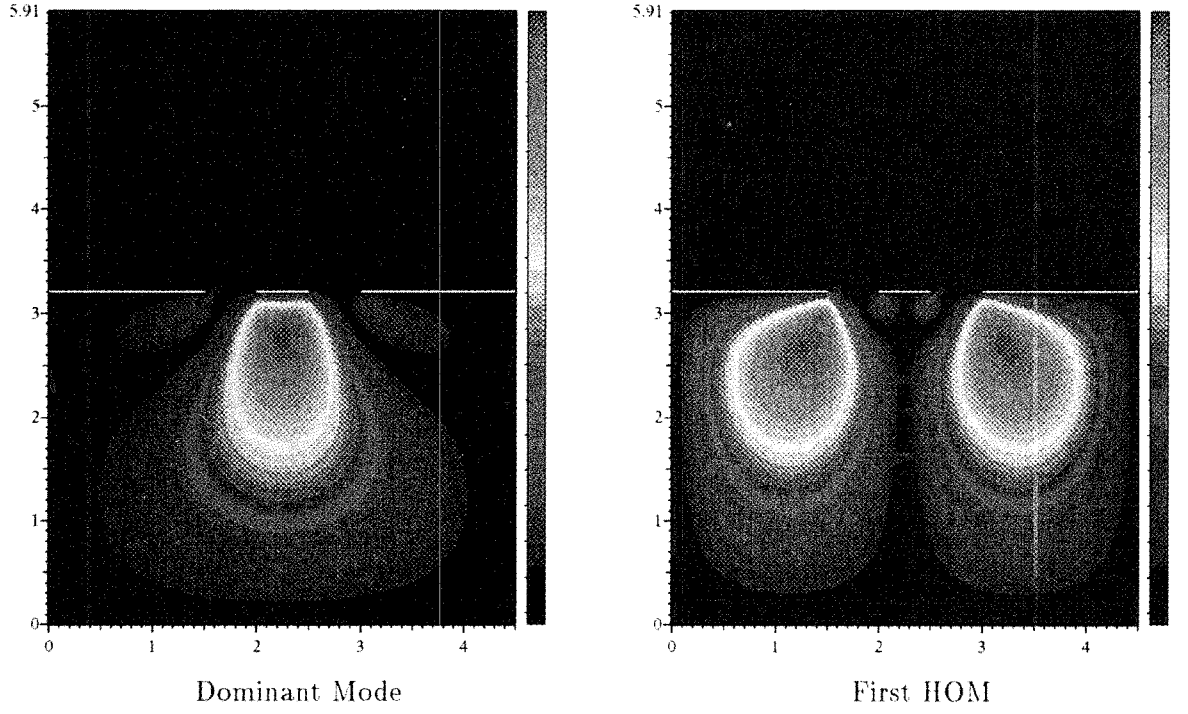

Fig. 10. Longitudinal fields for the dominant mode and first HOM of a conventional CPW at a frequency of 15 GHz (all dimensions are in millimeters).

in ϵ_{reff} as θ varies from 0 to 90° is primarily due to the fact that $\epsilon_{yy} > \epsilon_{xx}$ for this material. In addition to the more dispersive dominant mode, the gap between the two modes becomes narrower which clearly results in a much stronger coupling between them. On the other hand, also illustrated in Fig. 9, the overall effect of rotation on the characteristic impedance of the two modes is relatively small. Thus, crystal rotation effects for the case of sapphire will not improve the propagation characteristics of the structure, at least as far as coupling and dispersion is concerned.

For the remaining three types of crystals, i.e., epsilam-10, boron nitride, and PTFE cloth, the effect of rotating the crystal lattice is quite opposite to that of sapphire. By rotating the crystal, the effective dielectric constant of the dominant mode decreases considerably, thereby improving the dispersion characteristics of the structure. This decrease in ϵ_{reff} as θ increases is due to the fact that $\epsilon_{yy} < \epsilon_{xx}$ for these materials. In addition, a considerable decrease in the coupling between the two most dominant modes is also observed as the angle of rotation varies from 0° to 90°. The total percent change in the ϵ_{reff} of the dominant mode at 50 GHz, as the crystal lattice is rotated by 90°, is summarized in Table II.

A more complete understanding of the existing modes in a particular structure is usually obtained through data visualization of the field components. At a frequency of 15 GHz, typical contour plots of the longitudinal fields for the dominant and first higher order modes were generated for each CPW structure using a boron nitride substrate. The dominant and first higher order modes of the conventional CPW are depicted in Fig. 10, while those of the suspended CPW are shown in Fig. 11. For both modes, the contour plots demonstrate that most of the longitudinal fields are concentrated within the substrate material of each CPW configuration. The symmetric nature of both CPW structures along the vertical direction is also illustrated in these figures. A distinctive characteristic of the dominant mode is that of a perfect magnetic wall (PMC) across the line of symmetry; in contrast, the first higher order mode is characterized by a perfect electric wall (PEC). As illustrated in Fig. 10, for the conventional CPW, the longitudinal fields are spread throughout the entire substrate, whereas in Fig. 11, for the suspended CPW, the fields are compressed toward the substrate interface, thus, resulting in a less dispersive structure.

IV. Conclusion

A suitable vector-nodal finite element formulation, which incorporates both electric and magnetic biaxial and transverse plane anisotropies, was presented and applied to several common MMIC structures. In addition, a convenient characteristic impedance formulation using linear triangular finite elements and a power-voltage definition was presented. The resulting generalized eigenvalue problem was solved efficiently using a forward iteration algorithm while taking full advantage of the sparsity of the matrices.

Numerical results of the effective dielectric constant and characteristic impedance of several MMIC structures using electric and magnetic anisotropic substrates were compared with existing published data and show very good agreement. Two specific geometries, conventional and suspended CPW's,

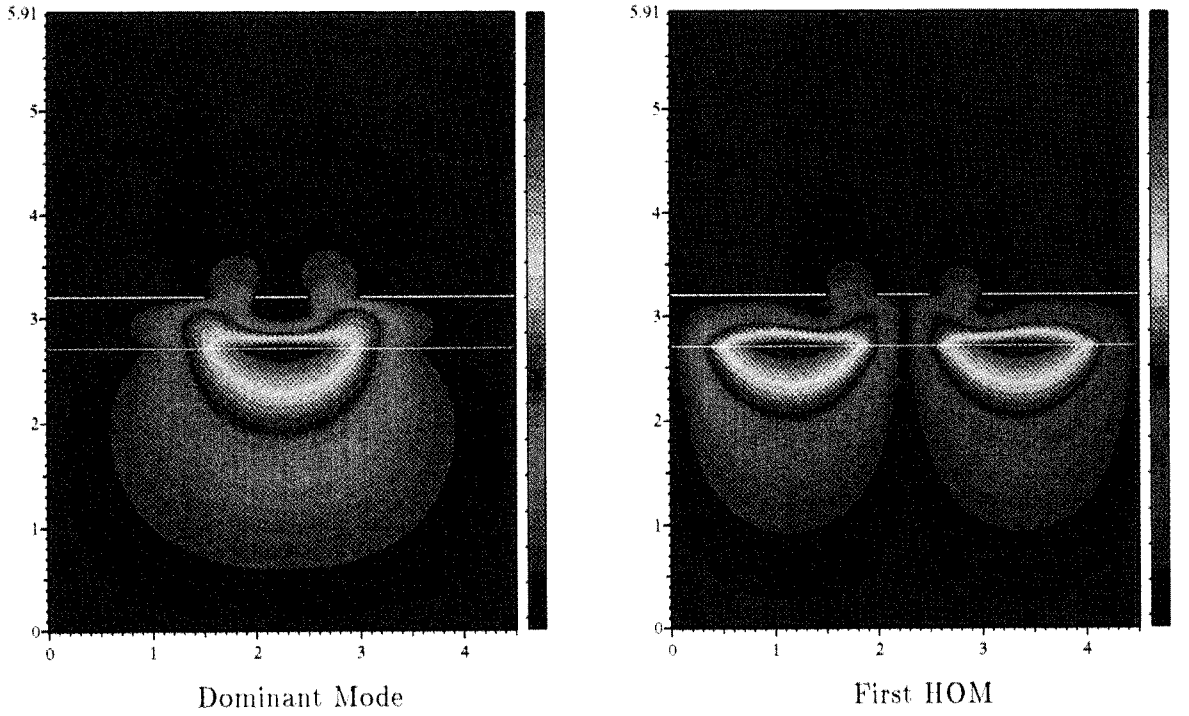

Fig. 11. Longitudinal fields for the dominant mode and first HOM of a suspended CPW at a frequency of 15 GHz (all dimensions are in millimeters).

were analyzed using four common anisotropic materials. It was found that the suspended CPW exhibited much less dispersion and mode interaction compared to the conventional CPW configuration. The cutoff frequencies of the HOM's are also shifted to higher values with the potential for increasing single mode operational bandwidth. In addition, a principal axis rotation was shown to further improve the dominant mode dispersion characteristics as well as dominant mode interaction with HOM's.

APPENDIX

Using the permittivity and permeability tensor definitions given in Section II, the corresponding elemental matrices of the finite element formulation when using linear triangular elements are given below:

$$[T_{tt}^e]_{11} = \frac{l_1^2}{24A}\left\{\epsilon_{xx}\left[b_3^2 - b_2b_3 + b_2^2\right] + (\epsilon_{xy}+\epsilon_{yx}) \cdot \left(b_3c_3 - \frac{b_2c_3 + c_2b_3}{2} + b_2c_2\right) + \epsilon_{yy}[c_3^2 - c_2c_3 + c_2^2]\right\} \tag{38}$$

$$[T_{tt}^e]_{22} = \frac{l_2^2}{24A}\left\{\epsilon_{xx}[b_1^2 - b_1b_3 + b_3^2] + (\epsilon_{xy}+\epsilon_{yx}) \cdot \left(b_1c_1 - \frac{b_1c_3 + c_1b_3}{2} + b_3c_3\right) + \epsilon_{yy}[c_1^2 - c_1c_3 + c_3^2]\right\} \tag{39}$$

$$[T_{tt}^e]_{33} = \frac{l_3^2}{24A}\left\{\epsilon_{xx}[b_2^2 - b_2b_1 + b_1^2] + (\epsilon_{xy}+\epsilon_{yx}) \cdot \left(b_2c_2 - \frac{b_2c_1 + c_2b_1}{2} + b_1c_1\right) + \epsilon_{yy}[c_2^2 - c_2c_1 + c_1^2]\right\} \tag{40}$$

$$[T_{tt}^e]_{12} = \frac{l_1l_2}{24A}\left[\epsilon_{xx}\left(\frac{b_3b_1 - b_3^2 + b_2b_3}{2} - b_2b_1\right) + \epsilon_{xy}\left(\frac{b_3c_1 - b_3c_3 + b_2c_3}{2} - b_2c_1\right) + \epsilon_{yx}\left(\frac{b_1c_3 - b_3c_3 + b_3c_2}{2} - b_1c_2\right) + \epsilon_{yy}\left(\frac{c_3c_1 - c_3^2 + c_2c_3}{2} - c_2c_1\right)\right\} \tag{41}$$

$$[T_{tt}^e]_{21} = [T_{tt}^e]_{12} \quad \text{where} \quad \begin{cases}\epsilon_{xy} \rightarrow \epsilon_{yx}\\ \epsilon_{yx} \rightarrow \epsilon_{xy}\end{cases} \tag{42}$$

$$[T_{tt}^e]_{13} = \frac{l_1l_3}{24A}\left[\epsilon_{xx}\left(\frac{b_3b_2 - b_2^2 + b_2b_1}{2} - b_3b_1\right) + \epsilon_{xy}\left(\frac{b_3c_2 - b_2c_2 + b_2c_1}{2} - b_3c_1\right) + \epsilon_{yx}\left(\frac{b_2c_3 - b_2c_2 + b_1c_2}{2} - b_1c_3\right) + \epsilon_{yy}\left(\frac{c_3c_2 - c_2^2 + c_2c_1}{2} - c_3c_1\right)\right] \tag{43}$$

$$[T_{tt}^e]_{31} = [T_{tt}^e]_{13} \quad \text{where} \quad \begin{cases}\epsilon_{xy} \rightarrow \epsilon_{yx}\\ \epsilon_{yx} \rightarrow \epsilon_{xy}\end{cases} \tag{44}$$

$$[T_{tt}^e]_{23} = \frac{l_2l_3}{24A}\left[\epsilon_{xx}\left(\frac{b_1b_2 - b_1^2 + b_3b_1}{2} - b_3b_2\right) + \epsilon_{xy}\left(\frac{b_1c_2 - b_1c_1 + b_3c_1}{2} - b_3c_2\right)\right.$$

$$+\epsilon_{yx}\left(\frac{b_2c_1-b_1c_1+b_1c_3}{2}-b_2c_3\right)+\epsilon_{yy}\left(\frac{c_1c_2-c_1^2+c_3c_1}{2}-c_3c_2\right)\Bigg] \quad (45)$$

$$[T^e_{tt}]_{32}=[T^e_{tt}]_{23} \quad \text{where} \quad \begin{cases}\epsilon_{xy}\rightarrow\epsilon_{yx}\\ \epsilon_{yx}\rightarrow\epsilon_{xy}\end{cases} \quad (46)$$

$$[S^e_{tt}]_{ij}=\mu^{inv}_{zz}\frac{l_il_j}{A} \quad i=1,\cdots,3;\ j=1,\cdots,3 \quad (47)$$

$$[B^e_{tz}]_{1j}=\frac{l_1}{12A}[b_j(b_3-b_2)\mu^{inv}_{yy}+c_j(c_3-c_2)\mu^{inv}_{xx}-c_j(b_3-b_2)\mu^{inv}_{yx}-b_j(c_3-c_2)\mu^{inv}_{xy}] \quad j=1,\cdots,3 \quad (48)$$

$$[B^e_{tz}]_{2j}=\frac{l_2}{12A}[b_j(b_1-b_3)\mu^{inv}_{yy}+c_j(c_1-c_3)\mu^{inv}_{xx}-c_j(b_1-b_3)\mu^{inv}_{yx}-b_j(c_1-c_3)\mu^{inv}_{xy}] \quad j=1,\cdots,3 \quad (49)$$

$$[B^e_{tz}]_{3j}=\frac{l_3}{12A}[b_j(b_2-b_1)\mu^{inv}_{yy}+c_j(c_2-c_1)\mu^{inv}_{xx}-c_j(b_2-b_1)\mu^{inv}_{yx}-b_j(c_2-c_1)\mu^{inv}_{xy}] \quad j=1,\cdots,3 \quad (50)$$

$$[B^e_{zt}]_{ij}=[B^e_{tz}]_{ji} \quad \text{where} \quad \begin{cases}\mu^{inv}_{xy}\rightarrow\mu^{inv}_{yx}\\ \mu^{inv}_{yx}\rightarrow\mu^{inv}_{xy}\end{cases} \quad i=1,\cdots,3;\ j=1,\cdots,3 \quad (51)$$

$$[S^e_{zz}]_{ij}=\frac{1}{4A}[b_ib_j\mu^{inv}_{yy}+c_ic_j\mu^{inv}_{xx}-b_ic_j\mu^{inv}_{yx}-c_ib_j\mu^{inv}_{xy}] \quad i=1,\cdots,3;\ j=1,\cdots,3 \quad (52)$$

$$[T^e_{zz}]_{ij}=\frac{A}{12}(1+\delta_{ij})\epsilon_{zz} \quad \delta_{ij}=\begin{cases}1 & \text{if } i=j\\ 0 & \text{otherwise}\end{cases} \quad i=1,\cdots,3;\ j=1,\cdots,3 \quad (53)$$

ACKNOWLEDGMENT

The authors would like to thank Dr. J. F. Harvey of the Electronics Division, Army Research Office, and Dr. J. W. Mink, formerly of ARO, for their interest and support of the project.

REFERENCES

[1] N. G. Alexopoulos, "Integrated-circuit structures on anisotropic substrates," *IEEE Trans. Microwave Theory Tech.*, vol. MTT-33, pp. 847–881, Oct. 1985.

[2] Y. Chen and B. Beker, "Dispersion characteristics of open and shielded microstrip lines under a combined principal axes rotation of electrically and magnetically anisotropic substrates," *IEEE Trans. Microwave Theory Tech.*, vol. 41, pp. 673–679, Apr. 1993.

[3] G. Mazé-Merceur, S. Tedjini, and J.-L. Bonnefoy, "Analysis of a CPW on electric and magnetic biaxial substrate," *IEEE Trans. Microwave Theory Tech.*, vol. 41, pp. 457–461, Mar. 1993.

[4] A. A. Mostafa, C. M. Krowne, and K. A. Zaki, "Numerical spectral matrix method for propagation in general layered media: Application to isotropic and anisotropic substrates," *IEEE Trans. Microwave Theory Tech.*, vol. MTT-35, pp. 1399–1407, Dec. 1987.

[5] R. R. Mansour and R. H. Macphie, "A unified hybrid-mode analysis for planar transmission lines with multilayer isotropic/anisotropic substrates," *IEEE Trans. Microwave Theory Tech.*, vol. MTT-35, pp. 1382–1391, Dec. 1987.

[6] J. B. Davies and D. Mirshekar-Syahkal, "Spectral domain solution of arbitrary coplanar transmission line with multilayer substrate," *IEEE Trans. Microwave Theory Tech.*, vol. MTT-25, pp. 143–146, Feb. 1977.

[7] M. Riaziat, R. Majidi-Ahy, and I. J. Feng, "Propagation modes and dispersion characteristics of coplanar waveguides," *IEEE Trans. Microwave Theory Tech.*, vol. 38, pp. 245–251, Mar. 1990.

[8] Y. Qian, E. Yamashita, and K. Atsuki, "Modal dispersion control and distortion suppression of picosecond pulses in suspended coplanar waveguides," *IEEE Trans. Microwave Theory Tech.*, vol. 40, pp. 1903–1909, Oct. 1992.

[9] C. N. Chang, W. C. Chang, and C. H. Chen, "Full wave analysis of multilayer coplanar lines," *IEEE Trans. Microwave Theory Tech.*, vol. 39, pp. 747–750, Apr. 1991.

[10] M. R. Lyons, J. P. K. Gilb, and C. A. Balanis, "Enhanced dominant mode operation of a shielded multilayer coplanar waveguide via substrate compensation," *IEEE Trans. Microwave Theory Tech.*, vol. 41, pp. 1564–1567, Sept. 1993.

[11] T. Kitazawa and R. Mittra, "Quasistatic characteristics of asymmetrical and coupled coplanar-type transmission lines," *IEEE Trans. Microwave Theory Tech.*, vol. MTT-33, pp. 771–778, Sept. 1985.

[12] J. F. Lee, D. Sun, and Z. J. Cendes, "Full-wave analysis of dielectric waveguides using tangential vector finite elements," *IEEE Trans. Microwave Theory Tech.*, vol. 39, pp. 1262–1271, Aug. 1991.

[13] Y. Lu and A. Fernandez, "An efficient finite element solution of inhomogeneous anisotropic and lossy dielectric," *IEEE Trans. Microwave Theory Tech.*, pp. 1215–1223, June/July 1993.

[14] K. Hayata, K. Miura, and M. Koshiba, "Finite element formulation for lossy waveguides," *IEEE Trans. Microwave Theory Tech.*, vol. MTT-36, pp. 268–276, Feb. 1988.

[15] G. H. Golub and C. F. Van Loan, *Matrix Computations.* Baltimore: Johns Hopkins Press, 1989.

[16] B. T. Smith *et al., Matrix Eigensystem Routines—EISPACK Guide.* New York: Springer-Verlag, 1976.

[17] K. S. Kundert and A. Sangiovanni-Vincentelli, *Sparse User's Guide: A Sparse Linear Equation Solver, ver. 1.3a,* University of California, Berkeley, Berkeley, CA 94720, 1988.

[18] "SDRC I-DEAS," Structural Dynamics Research Corporation, 2000 Eastman Dr., Milford, OH 45150, (513) 576-2400.

[19] S. J. Chung and L. K. Wu, "Analysis of the effects of a resistively coated upper dielectric layer on the propagation characteristics of hybrid modes in a waveguide-shielded microstrip using the method of lines," *IEEE Trans. Microwave Theory Tech.*, vol. 41, pp. 1393–1399, Aug. 1993.

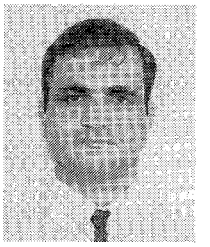

Anastasis C. Polycarpou (SM'94) was born in Nicosia, Cyprus, in October 1967. He received the B.S. degree in electrical engineering, *summa cum laude*, from Arizona State University, Tempe, AZ, in 1992. In 1994, he received the M.S. degree in electrical engineering. He is currently pursuing the Ph.D. degree in the same university.

He later joined the Telecommunications Research Center (TRC) at Arizona State University as a Graduate Student Research Assistant. His research interests include analytical and computational electromagnetics applied to MMIC structures, wave propagation, and scattering as well as antenna radiation.

Michael R. Lyons (S'94) was born in Los Alamos, NM, in 1968. He received the B.S.E.E. degree in electrical engineering from New Mexico State University, Las Cruces, NM, in 1991. He received the M.S.E.E. degree in 1994. He is currently pursuing the Ph.D. degree in electrical engineering at Arizona State University, Tempe, AZ.

He is with the Telecommunications Research Center at Arizona State University. His current research interests include full-wave modeling of packaging and interconnects in MMIC's and the application of hybrid numerical techniques in electromagnetics.

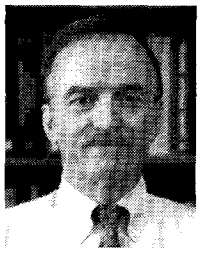

Constantine A. Balanis (S'62–M'68–SM'74–F'86) received the B.S.E.E. degree from Virginia Tech, Blacksburg, VA, in 1964, the M.E.E. degree from the University of Virginia, Charlottesville, VA, in 1996, and the Ph.D. degree in electrical engineering from Ohio State University, Columbus, OH, in 1969.

From 1964 to 1970, he was with NASA Langley Research Center, Hampton VA, and from 1970 to 1983 he was with the Department of Electrical Engineering, West Virginia University, Morgantown, WV. Since 1983 he has been with the Department of Electrical Engineering, Arizona State University, Tempe, AZ, where he is now Regent's Professor and Director of the Telecommunications Research Center. His research interests are in low- and high-frequency computational methods for antennas, scattering, and penetration; transient analysis, control of coupling, and reduction of pulse distortion in interconnects for monolithic microwave and millimeter wave circuits and electronic packaging; and multipath propagation. He is the author of *Antenna Theory: Analysis and Design* (Wiley, 1982) and *Advanced Engineering Electromagnetics* (Wiley, 1989).

Dr. Balanis received the 1992 Special Professionalism Award from the IEEE Phoenix Section, the 1989 IEEE Region 6 Individual Achievement Award, and the 1987–1988 Graduate Teaching Excellence Award, School of Engineering, Arizona State University. He is a Fellow of the IEEE and a member of ASEE, Sigma Xi, Electromagnetics Academy, Tau Beta Pi, Eta Kappa Nu, and Phi Kappa Phi. He has served as Associate Editor of the IEEE TRANSACTIONS ON ANTENNAS AND PROPAGATION (1974–1977) and the IEEE TRANSACTIONS ON GEOSCIENCE AND REMOTE SENSING (1981–1984), as an Editor of the Newsletter for the IEEE Geoscience and Remote Sensing Society, and as Chairman of the Distinguished Lecturer Program of the IEEE Antennas and Propagation Society (1988–1991) and member of the AdCom (1992–1995) of the IEEE Antennas and Propagation Society.